Dalton Transactions

ROYAL SOCIETY OF CHEMISTRY

PAPER

View Article Online
View Journal | View Issue

Cite this: *Dalton Trans.*, 2025, **54**, 2799

Rationalization of the structural, electronic and photophysical properties of silver(I) halide *n*-picolylamine hybrid coordination polymers†

Caterina Zuffa, [a] Daniele Veclani, [b] Marianna Marchini, [a] Filippo Monti, *[b] Chiara Cappuccino,‡[a] Lucia Maini *[a] and Barbara Ventura [b]

Hybrid coordination polimers based on AgX (with X = Cl, Br) and 2-, 3-, 4-picolylamine ligands, obtained by means of solvent-free methods, show peculiar luminescence properties that are strongly influenced by their structural motif, which in turn is defined by the adopted isomer of the ligand. A comprehensive study, combining photophysical methods and DFT calculations, allowed to rationalize the emissive behaviour of such hybrid coordination polymers in relation to their crystal structures and electronic properties. By means of luminescence measurements at variable temperatures, the nature of the emissive excited states and their deactivation dynamics was interpreted, revealing XMLCT transitions in the $[(AgX)(2\text{-pica})]_n$ compounds, a TADF behaviour in the case of 3-pica derivatives, and a dual emission at room temperature for the $[(AgX)(4\text{-pica})]_n$ family. The presence of low energy CC states, permitted by argentophilic interactions, is also considered in $[(AgX)(2\text{-pica})]_n$, whose structures are characterized by single/double inorganic chains, and in $[(AgX)(4\text{-pica})]_n$, where discrete dimeric Ag_2X_2 units are present. These findings open new avenues for the design and application of luminescent AgX-based hybrid materials.

Received 28th October 2024,
Accepted 25th December 2024

DOI: 10.1039/d4dt03003f

rsc.li/dalton

Introduction

The luminescence of d^{10} metal complexes has been intensely explored in the past decades, showing interesting characteristics that depend on the different excited states that can be involved in the radiative process and on the possibility of tuning these states not only by different ligand selection,[1–4] but also taking advantage of thermo- and/or mechanochromism.[5–14] The study of Cu(I)-halide containing complexes, in particular, has been seminal, leading to unveil characteristic halide-to-ligand charge transfer (XLCT) and cluster-centred (CC) emissive states, the latter related to transitions localized on the Cu_4I_4 core and possible only in the presence of metallophilic interactions.[15–20] Recently, several copper(I) compounds were also found to show the so-called thermally activated delayed fluorescence.[21–24]

In this context, however, the luminescence properties of coordination compounds based on silver(I)-halide have not been extensively investigated, if compared to those of parent copper(I)- and gold(I)-based analogues. This could be mainly due to their higher photosensitivity, which makes their characterization difficult.[25] As for CuX-based coordination polymers,[26–34] also in the case of AgX-based materials the photoluminescence properties have been studied principally for polymeric structures.[35–40] The nature of the emission displayed by these compounds has been found difficult to rationalize and, considering that there are only few studies on silver halide-based coordination polymers, the exploration of new systems and the careful investigation of their photophysical properties remain an important challenge.

From the structural point of view, AgX-based compounds mainly present a tetrahedrally coordinated silver atom but the possibility of the halogen to act as μ (bridging) ligand[1–5] allows a great variability of structures.[36] The nuclearity of the inorganic units can be used to pinpoint two different families: (i) discrete inorganic fragments, where the presence of an organic ligand (acting as a bridge) allows the creation of coordination polymers or/and MOFs,[41] and (ii) infinite inorganic units, where the polymeric expansion is due to the inorganic part and the presence of bridging organic ligands can

[a]*Università di Bologna, Dipartimento di Chimica "Giacomo Ciamician", Via F. Selmi 2, 40126 Bologna, Italy. E-mail: l.maini@unibo.it*
[b]*Consiglio Nazionale delle Ricerche, Istituto per la Sintesi Organica e la Fotoreattività (CNR–ISOF), Via Piero Gobetti 101, 40129 Bologna, Italy. E-mail: filippo.monti@isof.cnr.it*

†Electronic supplementary information (ESI) available: Additional crystallographic, spectroscopic and theoretical data, thermogravimetric analysis and differential scanning calorimetry. CCDC 2362555–2362558. For ESI and crystallographic data in CIF or other electronic format see DOI: https://doi.org/10.1039/d4dt03003f

‡Present address: Chemistry Department, Brookhaven National Laboratory, Brookhaven, NY, USA.

increase the dimensionality. We refer to these latter compounds as hybrid coordination polymers (HCP).[36,42]

We have recently reported the synthesis and the structural characterization of AgX-based (X = I, Br) coordination polymers containing *n*-picolylamine (*n*-pica) ligands, finding indications that the AgBr derivatives were emissive.[36] Following this study, we focused our interest on the synthesis and characterization of coordination polymers derived from AgCl, in order to examine the influence of the halide on the crystal structure and on the luminescence properties of the final material. In the present work, we thus deepen the knowledge on compounds based on AgX and *n*-picolylamine (*n*-pica) as organic ligand, by including the newly prepared $[(AgCl)(n\text{-pica})]_n$ products and by implementing the photophysical study on the whole class of AgCl and AgBr compounds (the AgI derivatives were previously found to be non-emissive and thus not considered in the present work).

The new AgCl-based coordination polymers have been obtained reacting AgCl with the three isomers of the picolylamine: 2-, 3- and 4-pica. To overcome the poor solubility of the silver(I) halides we carried out the reactions by mechanochemistry, by slurry or by a simple contact between the two reagents (AgCl is solid, while the isomers of pica are all liquid).

Hereafter, we thus report on a complete structural, photophysical and theoretical study of a series of silver halide compounds ($[(AgX)(n\text{-pica})]_n$, with X = Cl and Br), where the properties of the materials have been investigated in terms of emission spectra at variable temperatures, excited-state lifetimes and emission quantum yields. A comprehensive density-functional-theory (DFT) investigation, coupled with periodic boundary conditions, allowed to support and interpret the experimental results.

Overall, the reported investigation provides important knowledge on the composition-structure-electronic relationships of luminescent silver halide complexes. In particular, our findings evidence the important role of the picolylamine isomer used as ligand in affecting the final luminescence properties of the materials. Noteworthy, for the first time in a class of AgX-based materials ($[(AgX)(4\text{-pica})]_n$), emission from CC states, allowed by the occurrence of argentophilic interactions, has been detected. These data are of particular importance in the current context of limited reports on the photophysical characterization of Ag(I)-based coordination polymers.

Results and discussion

Due to the low solubility of silver halide salts in almost every solvent, solution-based synthesis of related coordination polymers is prohibited. To overcome this problem, we directly ground the halide salt with the liquid ligand, *i.e.* the *n*-picolylamine, obtaining the coordination polymer with a high degree of crystallinity. The desired product could be also obtained by solvothermal synthesis, or slurry, or simply embedding the halide salt with the liquid ligand. These different methods were explored to obtain single crystals suitable for structure determination.

A recent datamining study[36] on AgXL structures (X = halide and L = organic ligand with N, P, As, O, S or Se) in the Cambridge structural database (CSD)[43] highlighted that the flexible coordination sphere of the silver ions is reduced to tetracoordinated Ag(I) in 81% of the structures. Further examination revealed that, in the AgCl subset, the chloride atom has a high tendency to form inorganic discrete units (88%), which can be observed in complexes as well in coordination polymers. In the small subset of HCP, chloride does not show any preference in the coordination number, and it is almost equally distributed as μ^2 (single chain), μ^3 (double chain) and $\mu^{>3}$. The structures obtained in the present study by reaction of AgCl with the isomers of the picolylamine are characterized by μ^2-Cl, which forms single chains, hence HCPs, in ($[[(AgCl)(2\text{-pica})]_n$ and $[(AgCl)(3\text{-pica})]_n$), while in ($[[(AgCl)(4\text{-pica})]_n$) it forms a discrete dimeric inorganic core and hence a classical coordination polymer.

For sake of clarity, the results are presented and discussed by grouping the compounds based on the *n*-pica ligand they contain and, within these sub-classes, the materials obtained with AgCl are compared to the ones based on bromide. This description allowed us to investigate the role of the organic ligand and the halogen on both structural and photophysical properties.

$[(AgX)(2\text{-pica})]_n$ with X = Cl, Br

The crystalline structure of $[(AgCl)(2\text{-pica})]_n$ was determined by SCXRD on a colourless, plate-like crystal obtained through solvothermal reaction. The structure is formed by infinite inorganic single chains of alternating silver(I) and chloride ions, running parallel to the *a* axis of the crystal cell (Fig. 1, left).

Within each chain, 2-pica molecules act as chelating ligands binding individual Ag(I) centres, which therefore display a distorted tetrahedral coordination. As a result, an independent 1-D network is found, and the single 1-D wires interact to each other through amino NH···Cl or CH···Cl intermolecular interactions. It is worth stating that such 1-D wires are helixes, leading to a chiral cell belonging to the orthorhombic $P2_12_12_1$ space group.

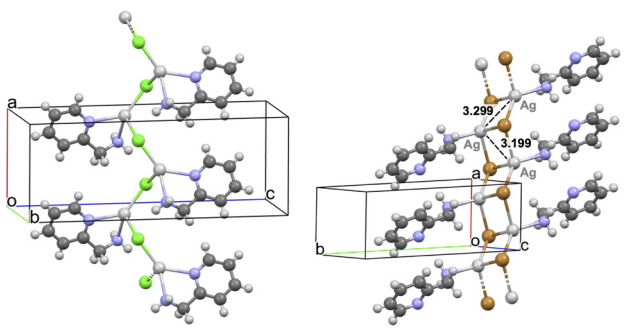

Fig. 1 Crystal structures of $[(AgCl)(2\text{-pica})]_n$ (left) and $[(AgBr)(2\text{-pica})]_n$ (right) showing their inorganic single- and double-chain, respectively, running parallel to the *a*-axis of their crystal cell (*a*-axis in red, *b*-axis in green, *c*-axis in blue).

$[(AgBr)(2\text{-pica})]_n$ is not isomorphic or isostructural to $[(AgCl)(2\text{-pica})]_n$ since it is characterized by an inorganic double chain, running parallel to the *a* axis of the crystal (Fig. 1, right). Moreover, the 2-pica ligands now bind silver(I) ions only through their amino group, while the pyridine moieties are uncoordinated. Notably, short Ag–Ag distances of 3.1989(9) and 3.2986(9) Å are found in the double chain of $[(AgBr)(2\text{-pica})]_n$, allowing argentophilic interactions.

Periodic DFT calculations, at the Perdew–Burke–Ernzerhof (PBE) level, have been carried out to investigate the structural and electronic properties of both crystals. Starting from the experimental X-ray structures, both the atoms and the cell parameters were fully relaxed preserving just the crystal space group and the cell symmetry. The obtained theoretical structures are compared to the experimental ones in Fig. S6,† showing a good agreement between them. As commonly found in literature,[44] the DFT-optimized structures display contracted unit cells due to the lack of thermal effects.

As far as the band structure of $[(AgCl)(2\text{-pica})]_n$ is concerned, the highest envelope of valence bands, spanning between −1.1 and −1.3 eV *vs.* the Fermi level, is predominantly constituted by σ* orbitals involving the 4d orbitals of silver(I) ions and the nitrogen lone pairs of the chelating 2-pica ligands, with minor contribution from chloride 3p orbitals (Fig. S7†). Such attribution can also be qualitatively inferred by comparing the band diagram and the partial density of states (DOS) reported in Fig. 2 bottom. The group velocity for these bands is very low in all reciprocal-space dimensions, confirming the strong localization of such orbitals. On the other hand, all lower-energy conduction bands are localized on the π* orbitals of the 2-pica ligands (Fig. S7†). Notably, the dispersion of such conduction bands is wider along a^* and b^* reciprocal directions, while it remains virtually zero along c^*, showing that the 1-D wires of $[(AgCl)(2\text{-pica})]_n$ are isolated along real-space *c* axis and display non-covalent interactions in the other two directions due to their herringbone packing (Fig. S8†).

In the case of $[(AgBr)(2\text{-pica})]_n$, all frontier valence bands are centred on the AgBr double chains and indeed display non-zero band widths only along k-paths having a^* components, since such chains run parallel to the *a* axis (Fig. 2 bottom and Fig. S9†). Frontier conduction bands are again centred on the π* orbitals of the 2-pica ligands; anyway, in the case of band #71 a non-negligible contribution from the inorganic double chain is observed (Fig. 2 bottom and Fig. S9†).

If compared to X-ray diffraction data, computed Ag–Ag distances in the inorganic double chain of $[(AgBr)(2\text{-pica})]_n$ are just slightly underestimated (*i.e.*, 2.889 and 2.968 Å *vs.* 3.199 and 3.299 Å). The presence of argentophilic interactions is further confirmed by the analysis of the mapped reduced density gradient (see Fig. S10† for further details). Furthermore, argentophilic interactions can be identified through the analysis of Raman spectra. Studies in literature

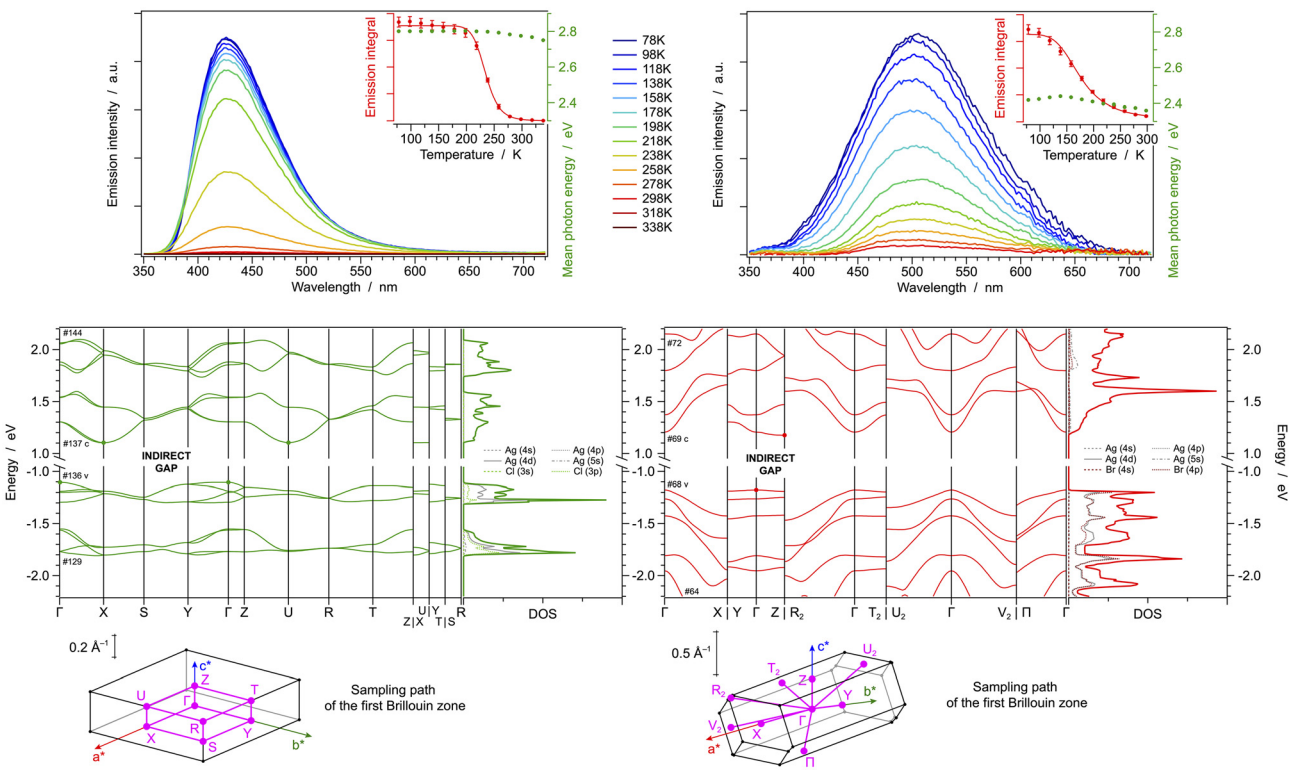

Fig. 2 (Top) Temperature-dependent emission spectra of $[(AgCl)(2\text{-pica})]_n$ (left) and $[(AgBr)(2\text{-pica})]_n$ (right), measured in the range between 78 and 338 K; the change in the emission intensity and mean-photon energy is also reported in the graph inset. (Bottom) Band-structure diagram and density-of-states (DOS) plot with relative orbital contributions; the band-structure path in the reciprocal space is also depicted.

indicate that, in the presence of such interactions, the ν(Ag–Ag) stretching frequency is typically observed within the range of 75–125 cm^{-1}.[45–50] Specifically, we attribute the peak at 81 cm^{-1} in the spectrum of $[(AgBr)(2\text{-pica})]_n$ (Fig. S20,† black line) to the stretching of Ag–Ag, confirming the presence of argentophilic interactions in this structure.

At room temperature, both crystals display the higher energy bands in their UV-vis absorption spectrum around 265 nm and a contribution at lower energy (Fig. S30,† left); Furthermore, they show an extremely weak and unstructured emission band, with maxima at 430 and 498 nm for $[(AgCl)(2\text{-pica})]_n$ and $[(AgBr)(2\text{-pica})]_n$, respectively (Table 1). The transition is expected to originate from a charge-transfer excited state of XMLCT nature, as suggested by DFT data. The emission intensity increases upon cooling to 78 K, but virtually no other spectral changes are observed (Fig. 2, top). Such a scenario is compatible with the presence of thermally activated non-radiative processes. Indeed, by monitoring the temperature-dependent emission intensity (insets of Fig. 2, top), it is possible to estimate the energy barrier that should be overcome to activate such processes; for $[(AgCl)(2\text{-pica})]_n$ a barrier of (0.38 ± 0.02) eV is estimated, while for $[(AgBr)(2\text{-pica})]_n$ a quenching is readily observed also at $T > 100$ K since the associated barrier is just (0.10 ± 0.01) eV (Fig. 2, top). Such effective quenching in $[(AgBr)(2\text{-pica})]_n$ can be tentatively explained considering the presence of easily accessible poorly radiative cluster-centred (CC) states, close to the XMLCT ones. Indeed, as indicated by the DOS plot (see above), a contribution from the empty AgBr-cluster orbitals is present at just 0.6 eV above the onset of the conduction bands.

$[(AgX)(3\text{-pica})]_n$ with X = Cl, Br

The structure of $[(AgCl)(3\text{-pica})]_n$ was solved by SCXRD on a colourless, plate-like crystal synthetized *via* contact reaction. The crystal belongs to the chiral monoclinic $P2_1$ space group and is characterized by single chains of alternating silver(I) and chloride ions, running parallel to the *b* axis of the crystal cell forming inorganic helixes (Fig. 3, left). This motif resembles the one already observed for $[(AgCl)(2\text{-pica})]_n$ but, in the present case, 3-pica binds two different inorganic chains generating a 2-D network. Due to the chiral group, the inorganic chains are all parallel and with the same direction of rotation.

Also $[(AgBr)(3\text{-pica})]_n$ shows a AgBr single chain generated by the screw axis and the 3-pica binding the inorganic chains forming the 2-D network. However, $[(AgBr)(3\text{-pica})]_n$ crystallizes as $P2_1/c$ space group and the parallel 2-D network is generated by the inversion centre, hence inorganic AgBr helixes of opposite chirality are present in the unit cell. Basically, both structures display equivalent 2-D networks stacked parallel to the *ab* crystal plane but, in the case of $[(AgCl)(3\text{-pica})]_n$, such 2-D layers are identical and created by a mere translation of the unit cell in *c* direction, while in $[(AgBr)(3\text{-pica})]_n$ nearby planes are enantiomeric and generated by inversion symmetry (Fig. 3).

The presence of the inversion centre slightly modifies the packing of the organic ligands, as show in Fig. 3 bottom: while in $[(AgCl)(3\text{-pica})]_n$ the ligands present only herringbone packing (Fig. 3, bottom left), in $[(AgBr)(3\text{-pica})]_n$ the interdigitated 3-pica ligands present herringbone and parallel arrangement (Fig. 3, bottom right). Someway, these two crystals can be considered as different polytypes of the more general $[(AgX)(3\text{-pica})]_n$ structure, considering its broadest definition.[51,52] Indeed, the similarity of the two structures, assessed by the isostructurality value (Is),[53] is 80% (see Experimental section for further details).[41,55]

To allow an easier comparison between the DFT computed structural and electronic properties of $[(AgCl)(3\text{-pica})]_n$ and $[(AgBr)(3\text{-pica})]_n$, a 1 × 1 × 2 supercell was considered for the former crystal. The fully optimized structures of both compounds are superimposed in Fig. S11,† clearly showing the

Table 1 Photoluminescence data of the coordination polymers $[(AgX)(2\text{-pica})]_n$, $[(AgX)(3\text{-pica})]_n$ and $[(AgX)(4\text{-pica})]_n$ (with X = Cl, Br) as powder at room temperature and at 78 K

	298 K			78 K	
	λ_{em}/nm	Φ_{em}(%)	τ/μs	λ_{em}/nm	τ/ms
$[(AgCl)(2\text{-pica})]_n$	430	0.1	—	426	68
$[(AgBr)(2\text{-pica})]_n$	498	<0.1	—	506	42
$[(AgCl)(3\text{-pica})]_n$	426	2.7	10.5	478	148
$[(AgBr)(3\text{-pica})]n$	436	1.2	9.2	482	108
$[(AgCl)(4\text{-pica})]_n$	450^{sh}, 520	1.6	10.1	480	287
$[(AgBr)(4\text{-pica})]_n$	425, 530	5.3	9.6, 13.2	484	425

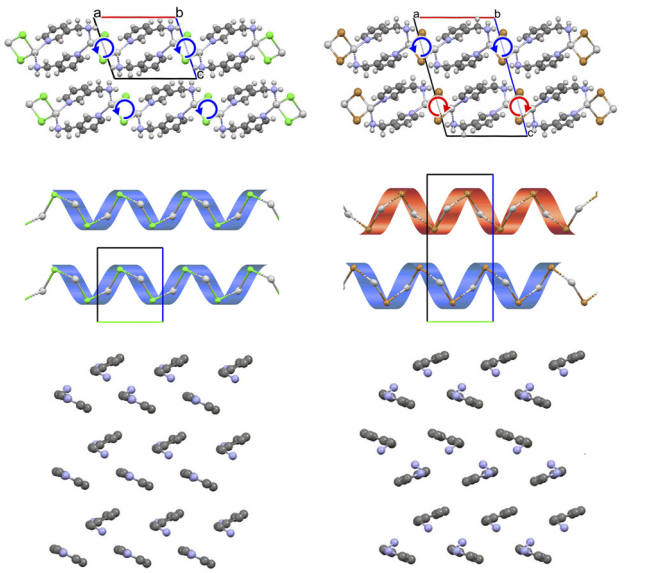

Fig. 3 (Top) Packing along *c*-axis of $[(AgCl)(3\text{-pica})]_n$ (left) and $[(AgBr)(3\text{-pica})]_n$ (right).[36] The directional arrows indicate the orientation of the "inorganic helices" (highlighted as black stripes in the middle). (Middle) packing along *a*-axis (the ligand is omitted for sake of clarity), which reveals the different direction of the chains. Cell axis color: *a* is red, *b* is green, and *c* is blue. (Bottom) the packing of 3-pica in the *bc* plane is illustrated for both $[(AgCl)(3\text{-pica})]_n$ (left) and $[(AgBr)(3\text{-pica})]_n$ (right). For clarity, hydrogen atoms are not shown.

presence of an inversion centre in the $[(AgBr)(3\text{-pica})]_n$ cell. As for the $[(AgX)(2\text{-pica})]_n$ series, the highest valence bands display the predominant contribution from the silver(I) 4d orbitals; however, the p orbitals of the halogen atoms always contribute to the valence bands in both $[(AgX)(3\text{-pica})]_n$ compounds. Not surprisingly, also in the present series, the lowest conduction bands are all centred on the π^* orbitals of the organic ligands.

Anyhow, for a proper comprehension of the band diagrams of these compounds it is useful to start discussing the spaghetti diagram of the smaller $[(AgCl)(3\text{-pica})]_n$ primitive cell (Fig. S12†), which already includes two equivalent [(AgCl)(3-pica)] units due to its C_2 point-group symmetry. Accordingly, all bands come in pairs, differing only for a phase change on equivalent orbitals. Since all the highest valence bands involve orbitals on the AgCl single helixes (running in the direction of the *b* axis) and two AgCl units are present in the cell, a huge energy change is expected if they are in phase or not. Consequently, within each pair, bands are well energy-separated in Γ, while they become degenerate when spanning the face of the first Brillouin zone having $b^*/2$ component (as in Z, D, E or C_2 *k*-points and related paths, see Fig. S12†). On the contrary, any change in the band momentum along a^* does not significantly perturb the bands because the inorganic wires are isolated by interdigitated 3-pica ligands (see Γ–Y_2 or Z–C_2 *k*-paths in Fig. S12†); the same is also observed for momentum changes with c^* components, albeit to a less extent, since the helixes (even if covalently separated) are more closely packed in that direction (see Γ–B or Z–D *k*-paths). A similar scenario is also observed for the lowest couple of conduction bands, ranging from 1.10 to 1.74 eV, since such bands are a linear combination of the two equivalent π^* orbitals on the 3-pica ligands (*i.e.*, the 3-pica LUMO); accordingly, their interactions are merely non-covalent (see Fig. S13† for a more complete discussion). The band diagram of $[(AgCl)(3\text{-pica})]_n$, depicted in Fig. 4, can be interpreted by analogy to the spaghetti diagram just discussed, simply considering that it refers to a 1 × 1 × 2 supercell.

As shown in Fig. 4 bottom, the band structure diagrams of $[(AgCl)(3\text{-pica})]_n$ and $[(AgBr)(3\text{-pica})]_n$ are very similar, if not for (i) the wider bandgap observed in the AgCl-based crystal and (ii) the removed fourfold degeneracy (along Z–D and E–Z–C_2 *k*-paths) in the conduction bands of $[(AgBr)(3\text{-pica})]_n$, which become a pair of two degenerate bands. Such a behavior is rationalized in Fig. S14† and can be understood considering the presence of different non-covalent interactions between the 3-pica ligands, coordinated to nearby AgBr helixes with different chirality (Fig. S15†).

Both compounds absorb in the spectral range 200–400 nm, with a maximum around 265 nm (Fig. S30,† middle), and are emissive at room temperature, displaying broad and unstructured profiles, as typical for XMLCT transitions (Fig. 4, top).

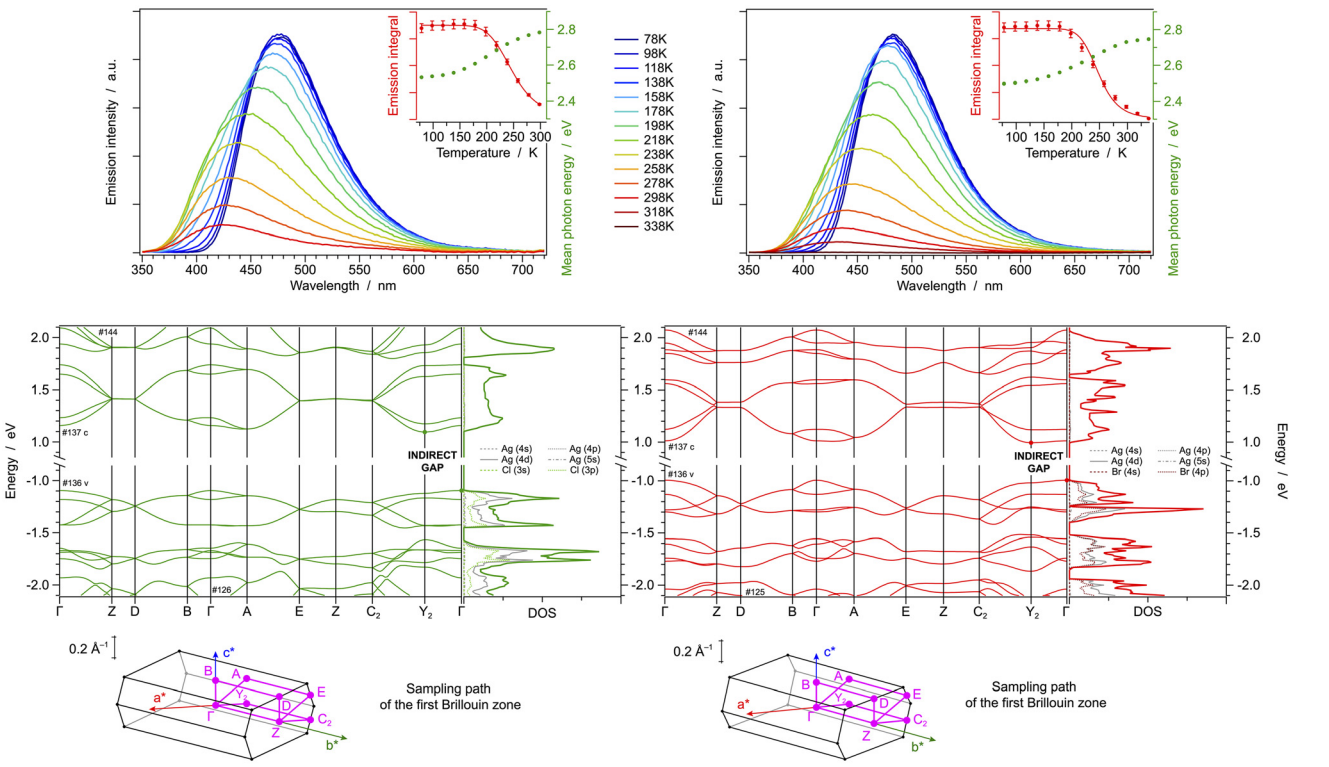

Fig. 4 (Top) Temperature-dependent emission spectra of $[(AgCl)(3\text{-pica})]_n$ (left) and $[(AgBr)(3\text{-pica})]_n$ (right), measured in the range between 78 and 338 K; the change in the emission intensity and mean-photon energy is also reported in the graph inset. (Bottom) Band-structure diagram and density-of-states (DOS) plot with relative orbital contributions; the band-structure path in the reciprocal space is also depicted. To allow the direct comparison of the two DFT-computed structures, a 1 × 1 × 2 supercell of $[(AgCl)(3\text{-pica})]_n$ is considered.

Photoluminescence quantum yields at 298 K are 2.7% and 1.2% for $[(AgCl)(3\text{-pica})]_n$ and $[(AgBr)(3\text{-pica})]_n$, respectively (Table 1). Remarkably, the emission band of $[(AgCl)(3\text{-pica})]_n$ is 10 nm blue shifted (λ_{max} = 426 *vs.* 436 nm for AgCl- *vs.* AgBr-derivative, Table 1). Such finding is in line with the band gap estimated by DFT calculations, which is 0.20 eV wider for $[(AgCl)(3\text{-pica})]_n$ (Fig. 4, bottom). On the contrary, at 78 K, the emission bands of both compounds are virtually superimposable, peaking at *ca.* 480 nm (Table 1) and preserving the same broad and unstructured profile as at room temperature. As shown in the inset of Fig. 4 top, the photon energy increase upon heating (*i.e.* the experimentally observed red shift upon cooling) can be taken as an indication of thermally activated delayed fluorescence (TADF), as typically reported for similar coordination structures.[9,54,55] The estimated singlet–triplet energy gap calculated by fitting the temperature-dependent emission intensity of both compounds (Fig. 4 top) is (0.22 ± 0.02) eV for $[(AgCl)(3\text{-pica})]_n$ and (0.30 ± 0.02) eV for $[(AgBr)(3\text{-pica})]_n$, which is comparable to the difference between the mean-photon energy at 78 K and the one at room temperature (approx. 0.25 and 0.23 eV, respectively; see insets of Fig. 4, top).

$[(AgX)(4\text{-pica})]_n$ with X = Cl, Br

The crystalline structure of $[(AgCl)(4\text{-pica})]_n$ was determined by simulated annealing on a XRPD pattern collected on a crystalline powder obtained by ball milling. The structure is isomorphous to the already reported $[(AgBr)(4\text{-pica})]_n$,[36] indeed, the two crystals show an index of cell similarity close to zero and the isostructurality index close to 100% (*i.e.*, π = 0.019 and Is = 98%, see Table S3†). Silver atoms display the typical tetrahedral coordination of Ag(I), binding two halogen atoms and two 4-pica ligands. Both structures present Ag_2X_2 units displaying short Ag–Ag distances (*i.e.*, 3.215 and 3.205 Å for Cl and Br compounds, respectively), suggesting argentophilic interactions. Such hypothesis is confirmed by Raman spectroscopy, showing peaks within the range between 75 and 125 cm^{-1} (Fig. S22†). Such Ag_2X_2 units are bridged together by the 4-pica ligands, which are linking one unit through their pyridine moiety and the other through the amino group (Fig. 5).

DFT calculations are in line with the experimental structural data obtained by X-ray diffraction, as demonstrated by the low RSMD values reported in Fig. S16.† Notably, the computed Ag–Ag distance in the Ag_2X_2 units is 3.158 and 2.995 Å for Cl and Br compounds, respectively. Moreover, the presence of an argentophilic interaction is further confirmed by reduced-density-gradient plot, as reported in Fig. S17.†

The similarity between the crystal structures of $[(AgCl)(4\text{-pica})]_n$ and $[(AgBr)(4\text{-pica})]_n$ is reflected in their similar band structures and in their virtually identical direct bandgap of 2.32 eV. As shown in the DOS plots of Fig. 6 bottom, the highest valence bands are mainly located on the Ag_2X_2 units, involving the 4d orbitals of the silver(I) ions and the valence p orbitals of the halogen atoms. As in previous cases, the lowest conduction bands are all centered on the π^* orbitals of the picolylamine ligands. These theoretical findings suggest that XMLCT transitions are estimated for both systems and, due to their identical direct bandgap, a bright emission at a similar wavelength is also expected.

The scenario predicted by DFT calculations is confirmed by experimental spectroscopic data at 78 K, where a broad and intense emission band centered at 480 and 484 nm is observed for $[(AgCl)(4\text{-pica})]_n$ and $[(AgBr)(4\text{-pica})]_n$, respectively (Fig. 6 top and Table 1); notably, such values correlate well with the calculated bandgap of 2.32 eV, corresponding to a transition at 534 nm. The photoluminescence quantum yields at 78 K are roughly estimated to be 27% for both compounds, as inferred by comparing the emission intensities at 78 K with the ones at 298 K (Fig. 6 top). The absorption spectrum of both compounds falls in the 200–500 nm spectral region with an envelope of bands between 250 and 350 nm and a low energy tail (Fig. S30,† right).

Temperature-dependent emission studies reveal a much more complicated picture as the temperature increases from 78 to 338 K (Fig. 6 top). For simplicity, the spectral evolution upon heating can be divided in two regions. In the temperature range between 78 and roughly 200 K only a broad emission band is present, corresponding to the XMLCT transition, which is gradually blue shifted upon increasing the temperature as typically observed in thermally activated delayed fluorescence (TADF) systems. Such a shift is more pronounced in the bromide than in the chloride HCP, as also indicated in the mean-photon energy graph (inset of Fig. 6 top). At 200 K the mean-photon energy drastically decreases because of the appearance of the second broad band at lower energy, peaking

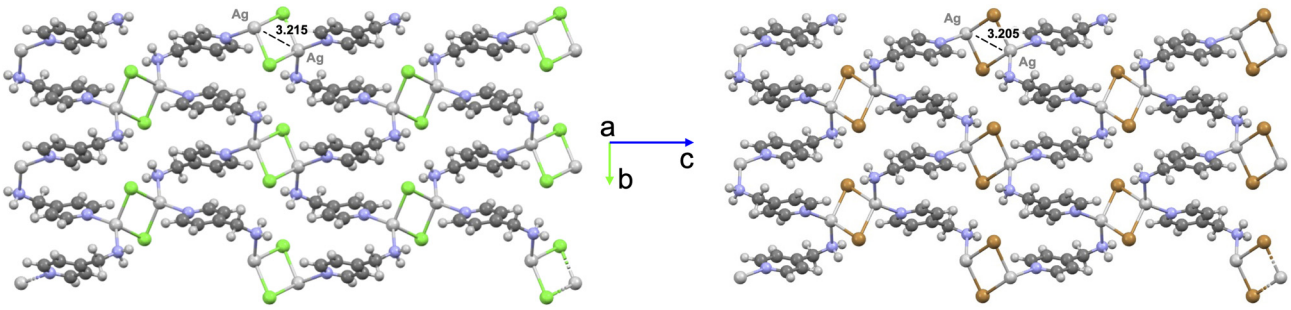

Fig. 5 Packing along *a*-axis of $[(AgCl)(4\text{-pica})]_n$ (left) and $[(AgBr)(4\text{-pica})]_n$ (right).

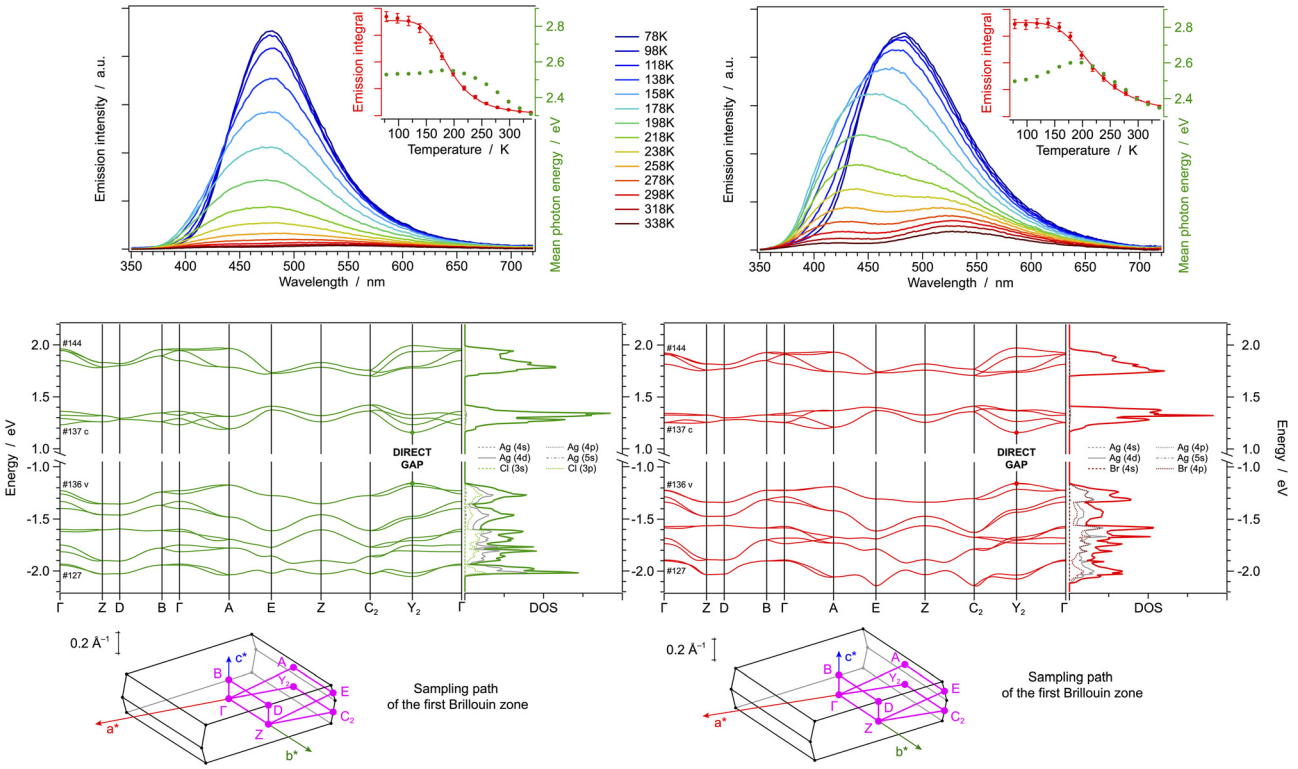

Fig. 6 (Top) Temperature-dependent emission spectra of $[(AgCl)(4\text{-pica})]_n$ (left) and $[(AgBr)(4\text{-pica})]_n$ (right), measured in the range between 78 and 338 K; the change in the emission intensity and mean-photon energy is also reported in the graph inset. (Bottom) Band-structure diagram and density-of-states (DOS) plot with relative orbital contributions; the band-structure path in the reciprocal space is also depicted.

around 530 nm for both systems. Such emission can be tentatively attributed to cluster-centered (CC) states located on the Ag_2X_2 units (Fig. S31†). Emissive CC states have been extensively documented for CuX based structures where short Cu–Cu distances allows interactions among the metal centers,[27,56,57] but, to the best of our knowledge, they have never been reported for Ag(I) halide based materials. In the present $[(AgX)(4\text{-pica})]_n$ compounds, CC emission is permitted by the presence of argentophilic interactions within the Ag_2X_2 discrete units of the structures.

The abovementioned interpretation of the temperature-dependent emission spectra is also corroborated by time-resolved measurements, since a sharp drop in excited-state lifetimes is clearly observed in $[(AgCl)(4\text{-pica})]_n$ and $[(AgBr)(4\text{-pica})]_n$, when passing from 78 K to 298 K (Table 1). Such a decrease in the emission lifetimes can be attributable to additional deactivation pathways: (i) the population of singlet excited states from long-living triplet ones, and (ii) the thermal activation of upper lying cluster-centered states, which typically display fast non-radiative deactivation to the ground state.[58,59]

Conclusions

We synthesized and characterized a series of three $[(AgCl)(n\text{-pica})]_n$ compounds and compared their photophysical properties with those of analogous compounds based on AgBr. The obtained structures are primarily HCP, which represent a minority family compared to the structures deposited in the CSD. We believe that our synthetic procedures (grinding or slurries) favour the HCP since they do not require the dissolution of the silver salt.

The obtained structures are compared in pairs containing the same organic ligand and different halogen atom.

The $[(AgX)(2\text{-pica})]_n$ compounds present very different structures depending on the halogen, while the similarities increase in the 3-pica compounds and with the 4-pica ligand the structures are isomorphic. The formation of an inorganic single chain promotes the presence of a chiral helix, which ends up in a chiral structure in $[(AgCl)(3\text{-pica})]_n$ and in 2-D chiral layers in $[(AgBr)(3\text{-pica})]_n$. The two latter structures differ only by the presence of the inversion centre in the bromide compound, which slightly changes the packing of the organic ligand. $[(AgX)(4\text{-pica})]_n$ (X = Cl, Br) are isomorphous and are characterized by discrete dimeric Ag_2X_2 units which favour the presence of short Ag–Ag distances.

The luminescence properties of these materials have been found to be mainly dependent on the isomer of the picolylamine ligand used, which also affects the final crystal structure. $[(AgX)(2\text{-pica})]_n$ compounds are the less emissive of the series at room temperature, while they display a bright emission at 77 K, in both cases attributed to XMLCT states. Such emissive

states are quenched, upon increasing the temperature, by thermally activated non-radiative processes.

The $[(AgX)(3\text{-pica})]_n$ complexes share the same 2-D network, despite the slight difference in their crystal structure, and indeed present a similar band diagram and comparable luminescence properties. These HCPs display higher quantum yields at RT compared to the $[(AgX)(2\text{-pica})]_n$ series and show a temperature-dependent red shift with increased emission intensity upon cooling. This behaviour has been rationalized in terms of a TADF process involving closely lying XMLCT states of singlet and triplet spin multiplicity.

Interestingly, the isomorphic $[(AgX)(4\text{-pica})]_n$ compounds show a dual emission at RT, while only one band at 78 K. Temperature-dependent investigations evidence a TADF process from 78 to 200 K involving XMLCT states and the population of CC emissive states above 200 K. The nature of the emissive state is clearly influenced by the presence of the chloride or bromide halogen. At 78 K the bromide promotes longer lifetimes and a more pronounced blue shift upon heating, which is almost negligible in $[(AgCl)(4\text{-pica})]_n$.

This comprehensive investigation combines structural, photophysical, and theoretical approaches to reveal structure–property relationships in hybrid coordination polymers based on silver(I) halides. As expected, the crystal structure of the HCP plays a crucial a role in the photophysical properties. Indeed, the presence of bromide favour argentophilic interactions, allowing accessible CC states. Our results suggest that these compounds, previously underexplored due to synthetic challenges now addressed through solvent-free processes, hold significant potential as luminescent materials for lighting and sensing applications.

Experimental section

Knowledge discovery on database

The probability of obtaining AgX-based hybrid coordination polymers was checked using the ConQuest software.[60] We examined the role of the halide in compounds AgXL – where X = Cl, Br, or I and L is an organic ligand with the atom binding directly to silver being N, P, As, O, S, or Se – deposited in the Cambridge structural database (CSD),[43] version 5.43 released in November 2021. In this way we selected the subset_AgXL that includes about 800 structures. For details on the selection procedure see the ESI.†[36]

Synthesis

All the reagents were purchased from Tokyo Chemical Industry (TCI) and employed without additional purification, except for AgCl which was synthesized from an aqueous solution of $AgNO_3$ and a saturated aqueous solution of NaCl. AgCl is solid and all the ligands (2-, 3- and 4-picolylamine, here called 2-, 3- and 4-pica) are in liquid form. All the reactions have been performed in a vessel covered with aluminum foil to prevent degradation, since both the silver halide reagent and the obtained products were found to be photosensitive.

Synthesis of $[(AgCl)(n\text{-pica})]_n$

Contact reaction. 1 mmol of AgCl (0.143 g) was covered with 1 mmol of *n*-pica (0.1 mL) in a glass vessel, mixed a little with a spatula and left still in the dark for at least 14 days. We obtained plate-shape single crystals of $[(AgCl)(2\text{-pica})]_n$ and $[(AgCl)(3\text{-pica})]_n$ and a crystalline powder of $[(AgCl)(4\text{-pica})]_n$, the latter non-suitable for SCXRD analysis.

Mechanochemical reaction. 1 mmol of AgCl (0.143 g) and 1 mmol of *n*-pica (0.1 mL) were placed in a 5 mL agate ball-milling jar with one agate sphere (5 mm diameter) and milled at 20 Hz for 60 minutes with Retsch MM200 vibratory mill equipped with horizontally oscillating arms. The obtained crystalline powders were washed with acetonitrile to eliminated unreacted *n*-pica and analysed with XRPD.

Slurry. 1 mmol of AgCl (0.143 g) and 1 mmol of *n*-pica (0.1 mL) were placed in a glass vessel with 1.5 mL of acetonitrile and the slurry was stirred in the dark (by covering the vessel with aluminium foil) for 24 hours. Crystalline powders were washed with acetonitrile. The XRPD patterns did not show unreacted AgCl.

Solvothermal reaction. 1 mmol of AgCl (0.143 g), 1 mmol of *n*-pica (0.1 mL) and 2 mL of acetonitrile or THF were placed in a 5 mL vial. Everything was put in a metal autoclave and placed in the stove at 90 °C for 24 hours. After that, the temperature has been diminished 9 °C h^{-1} until the room temperature was reached. We obtained crystals suitable for SCXRD analysis of the desired structures $[(AgCl)(2\text{-pica})]_n$ and $[(AgCl)(3\text{-pica})]_n$. In the case of the solvothermal reaction between AgCl and 4-pica, single crystals of $[Ag(H\text{-}4\text{-pica})Cl_2]_n$ were obtained, as detailed in the ESI.† The structure is reported (see ESI†) without further investigation.

Structure determination by X-ray diffraction

The single crystal data of $[(AgCl)(2\text{-pica})]_n$ and $[(AgCl)(3\text{-pica})]_n$ were collected at room temperature on an Oxford Xcalibur using Mo-ka radiation, equipped with graphite monochromator and CCD Sapphire detector. Crystal data details are summarized in Tables S1 and S2 in ESI.† The SHELXT[61] and SHELXL[62] algorithms were used for the solution and refinement of the structures based on F^2. All the atoms, excluding the hydrogens, were refined anisotropically. Hydrogen atoms have been added to the theoretical positions. The structure of $[(AgCl)(4\text{-pica})]_n$ was solved by X-ray powder diffraction. The powder data were obtained on a Panalytical X'Pert PRO using Cu-ka radiation, endowed with a focusing mirror, Pixcel Detector, and capillary holder. The sample was loaded in a 0.5 mm glass capillary. The analysis was carried out in transmission and collected in the range 2θ 5–70°, with 0.02 rad soller, $\frac{1}{4}$° divergence slit and $\frac{1}{4}$° antiscatter slit, step size 0.0131° and counting time of 168.045 s. Six consecutive repetitions of the same measurement were collected and merged to obtain an optimal ratio between the signal and the noise. The analysis of the powder data was performed by the software TOPAS 6,[63] and a Chebyshev function and a pseudo-Voigt (TCHZ type) were used to fit the background and the peak

shape, respectively. The powders were indexed with the cell reported in Table S2.† The structure was determined by simulated annealing and refined by the Rietveld method. All the hydrogen atoms were fixed in calculated position. CCDC 2362555–2362558† contains the supplementary crystallographic data for this paper.[64]

Isostructurality calculation

We used the software MERCURY[64] to superimpose the similar structures in order to calculate the isostructurality geometric descriptors. The parameters used in this work are π and Is, the indexes of cell similarity and isostructurality, respectively:

$$\pi = \left| \frac{a+b+c}{a'+b'+c'} - 1 \right|$$

$$\mathrm{Is}_{(n)} = \left| \left[\sum \frac{(\Delta R_i)^2}{n} \right]^{\frac{1}{2}} - 1 \right| \times 100\%$$

where a, b, c and a', b', c' are the orthogonalized lattice parameters of the two compared structures; n is the number of the considered atoms, excluding hydrogens; and ΔR_i are the distance differences between their atomic coordinates. If two structures are greatly similar, π is almost zero and the Is value must be close to 100%. The RMSD (the root mean square of the distance differences of the corresponding atoms) and the maximum distance difference between the compared atoms (max D) have been calculated through the superimposition of the asymmetric units in Mercury. More information about these numbers is reported by Croitor *et al.*[53] To calculate the π parameter we used the Lödwin orthogonalization of the cell parameters.[65,66]

Thermogravimetric analysis (TGA)

Thermogravimetric analyses were performed using a PerkinElmer TGA7. The measurements were carried out under nitrogen flow in a temperature range of 30–350 °C with a 5 °C min^{-1} gradient. The results are presented and discussed in the ESI (Fig. S24–S26†).

Differential scanning calorimetry (DSC)

DSC measurements were performed using a PerkinElmer Diamond DSC-7 equipped with a PII intracooler. The temperature and enthalpy calibrations were performed with high purity standards (*n*-decane, benzene and indium). The samples in aluminum open pans were heated at 5 °C min^{-1} unless otherwise indicated. The results are presented and discussed in the ESI (Fig. S27–S29†).

Raman spectroscopy

The Raman spectra of powder samples were measured with a WITec's Raman microscope aplha300 R excited by a 532 nm PS laser. The Raman spectra of three random spots were collected for each sample.

Photophysical measurements

Absorption and emission determinations were performed on powder samples placed inside two quartz slides. Reflectance spectra were recorded using a PerkinElmer Lambda 950 UV/Vis/NIR spectrophotometer equipped with a 100 mm integrating sphere and converted into absorption spectra using the Kubelka–Munk function.[67,68] Uncorrected emission spectra were obtained with an Edinburgh Instruments FLS920 spectrometer equipped with a Peltier-cooled Hamamatsu R928 photomultiplier tube (spectral window: 185–850 nm). An Osram XBO xenon arc lamp (450 W) was used as the excitation light source. The corrected spectra were acquired by means of a calibration curve, obtained by using an Ocean Optics deuterium–halogen calibrated lamp (DH-3plus-CAL-EXT). For temperature-dependent measurements, the sample was mechanically dispersed on a quartz slide and placed inside an Oxford Optistat DN variable-temperature liquid-nitrogen cryostat (operating range: 77–500 K) equipped with an ITC5035 temperature controller and interfaced with the same Edinburgh FLS920 fluorimeter. The emission lifetimes (τ) were measured through the time-correlated single photon counting (TCSPC) technique using a HORIBA Jobin Yvon IBH FluoroHub controlling a spectrometer equipped with a pulsed NanoLED and/or SpectraLED excitation sources (λ_{exc} = 283/331 and 370 nm, respectively) and a red-sensitive Hamamatsu R-3237-01 PMT detector (spectral window: 185–850 nm). The analysis of the luminescence decay profiles was accomplished with the DAS6 Decay Analysis Software provided by the manufacturer, and the quality of the fit was assessed with the χ^2 value close to unity and with the residuals regularly distributed along the time axis. Absolute photoluminescence quantum yields were calculated using corrected emission spectra obtained from the Edinburgh FLS920 spectrometer, equipped with a barium sulfate coated integrating sphere (inner diameter: 4 in.), following the procedure described by Würth *et al.*[69] Estimated errors are 10% on exponential lifetimes, 20% on quantum yields, 20% on molar absorption coefficients and 3 nm on emission and absorption peaks.

DFT calculations

DFT calculations on all crystals were carried out using Quantum ESPRESSO 7.0, the open-source suite for quantum simulation of materials.[70–72] The PBEsol GGA exchange–correlation functional[73] was chosen in combination with the semiempirical Grimme's DFT-D3 dispersion corrections with zero damping,[74] to take into account possible non-covalent interactions. The pseudopotentials were directly taken from the SSSP Efficiency PBEsol pseudopotential library (version 1.1.2);[75,76] the kinetic energy cut-off of the wave function was set to 60 Ry and the one for charge density to 480 Ry, according to the adopted pseudopotential requirements. For all SCF calculations, the convergence threshold for self-consistency was set to 2.0×10^{-10} Ry times the number of atoms in the cell. The initial guess for the structure of each compound was based on the experimental single-crystal X-ray diffraction data (directly taken from CIF files). All struc-

tures were fully relaxed using a variable-cell approach, using the BFGS (Broyden–Fletcher–Goldfarb–Shanno) algorithm. During the optimization, the only imposed constraint was to keep the crystal space group consistent with the experimental one, but both the cell parameters and ions were adjusted to obtain the minimum-energy structure; convergence threshold on total energy was set to 1.0×10^{-5} Ry times the number of atoms in the cell, with forces acting on atoms below 1.0×10^{-4} Ry Bohr^{-1}. For optimizations, the values for the K-point grid were selected so that the *k*-point distance in the reciprocal space was 0.3 Å^{-1}, as implemented in the materials cloud platform.[77] The *k*-point grid sampling was increased to 0.2 Å^{-1} for a higher-quality single-point SCF (self-consistent field) calculation on the optimized structure. For density-of-state (DOS) calculations, an even denser *k*-point grid was adopted in the corresponding NSCF (non-self-consistent field) calculation, imposing a *k*-point distance of 0.1 Å^{-1}. In order to obtain the band-structure diagrams, the first Brillouin zone was mapped along specific paths connecting both high-symmetry points and points related to important π–π planes in the direct lattice; *k*-points along the paths were sampled with a resolution of 0.025 Å^{-1} using a home-made Python script. For all compounds, the Fermi level was placed in the middle of the bandgap and all energies were referred to it. Visualization of selected wavefunction contributions to the pseudo-charge density at specific K-points was accomplished by VESTA (version 3.5.8).[78]

Author contributions

Conceptualization: F.M., L.M., B.V.; investigation and data curation: C.Z., D.V., M.M., F.M., C.C.; methodology: D.V., F.M.; software: D.V., F.M.; validation: F.M., L.M., B.V.; supervision: L. M., B.V.; writing – original draft: all; writing – review and editing: all; funding acquisition: F.M., L.M., B.V.

Data availability

The data supporting this article have been included as part of the ESI.†

Crystallographic data of novel compounds have been deposited at the Cambridge Crystallographic Data Centre (CCDC) 2362555 for $[(AgCl)(2\text{-pica})]_n$, 2362556 for $[(AgCl)(H\text{-}4\text{-pica})]_n$, 2362557 for $[(AgCl)(4\text{-pica})]_n$ and 2362558 for $[(AgCl)(3\text{-pica})]_n$.†

Conflicts of interest

There are no conflicts to declare.

Acknowledgements

Italian CNR (project "Light Induced Processes"), University of Bologna and MUR are acknowledged for support. C. Z. thanks the University of Bologna for a PhD grant and the Marco Polo fellowship.

References

1 A. Barbieri, G. Accorsi and N. Armaroli, Luminescent complexes beyond the platinum group: The d^{10} avenue, *Chem. Commun.*, 2008, 2185–2193.
2 V. W. W. Yam, A. K. W. Chan and E. Y. H. Hong, Charge-transfer processes in metal complexes enable luminescence and memory functions, *Nat. Rev. Chem.*, 2020, **4**, 528–541.
3 C. Wegeberg and O. S. Wenger, Luminescent First-Row Transition Metal Complexes, *JACS Au*, 2021, **1**, 1860–1876.
4 M. Wallesch, D. Volz, D. M. Zink, U. Schepers, M. Nieger, T. Baumann and S. Bräse, Bright coppertunities: Multinuclear CuI complexes with N-P ligands and their applications, *Chem. – Eur. J.*, 2014, **20**, 6578–6590.
5 R. C. Zhang, J. J. Wang, J. C. Zhang, M. Q. Wang, M. Sun, F. Ding, D. J. Zhang and Y. L. An, Coordination-Induced Syntheses of Two Hybrid Framework Iodides: A Thermochromic Luminescent Thermometer, *Inorg. Chem.*, 2016, **55**, 7556–7563.
6 T. L. Yu, Y. M. Guo, G. X. Wu, X. F. Yang, M. Xue, Y. L. Fu and M. S. Wang, Recent progress of d^{10} iodoargentate(I)/iodocuprate(I) hybrids: Structural diversity, directed synthesis, and photochromic/thermochromic properties, *Coord. Chem. Rev.*, 2019, **397**, 91–111.
7 B. Li, H. T. Fan, S. Q. Zang, H. Y. Li and L. Y. Wang, Metal-containing crystalline luminescent thermochromic materials, *Coord. Chem. Rev.*, 2018, **377**, 307–329.
8 J. López, M. Murillo, G. Lifante-Pedrola, E. Cantelar, J. Gonzalez-Platas, U. R. Rodríguez-Mendoza and P. Amo-Ochoa, Multi-stimulus semiconductor Cu(I)-I-pyrimidine coordination polymer with thermo- and mechanochromic sensing, *CrystEngComm*, 2022, **24**, 341–349.
9 F. Farinella, L. Maini, P. P. Mazzeo, V. Fattori, F. Monti and D. Braga, White luminescence achieved by a multiple thermochromic emission in a hybrid organic-inorganic compound based on 3-picolylamine and copper(I) iodide, *Dalton Trans.*, 2016, **45**, 17939–17947.
10 A. Kobayashi, Y. Yoshida, M. Yoshida and M. Kato, Mechanochromic Switching between Delayed Fluorescence and Phosphorescence of Luminescent Coordination Polymers Composed of Dinuclear Copper(I) Iodide Rhombic Cores, *Chem. – Eur. J.*, 2018, **24**, 14750–14759.
11 J. Conesa-Egea, J. Gallardo-Martínez, S. Delgado, J. I. Martínez, J. Gonzalez-Platas, V. Fernández-Moreira, U. R. Rodríguez-Mendoza, P. Ocón, F. Zamora and P. Amo-Ochoa, Multistimuli Response Micro- and Nanolayers of a Coordination Polymer Based on Cu_2I_2 Chains Linked by 2-Aminopyrazine, *Small*, 2017, **13**, 1700965.
12 E. Cariati, E. Lucenti, C. Botta, U. Giovanella, D. Marinotto and S. Righetto, *Coord. Chem. Rev.*, 2016, **306**, 566–614.
13 S. Perruchas, X. F. L. Goff, S. Maron, I. Maurin, F. Guillen, A. Garcia, T. Gacoin and J. P. Boilot, Mechanochromic and

thermochromic luminescence of a copper iodide cluster, *J. Am. Chem. Soc.*, 2010, **132**, 10967–10969.

14 Q. Benito, X. F. Le Goff, S. Maron, A. Fargues, A. Garcia, C. Martineau, F. Taulelle, S. Kahlal, T. Gacoin, J. P. Boilot and S. Perruchas, Polymorphic copper iodide clusters: Insights into the mechanochromic luminescence properties, *J. Am. Chem. Soc.*, 2014, **136**, 11311–11320.

15 C. K. Ryu, M. Vitale and P. C. Ford, Photoluminescence Properties of the Structurally Analogous Tetranuclear Copper(I) Clusters $Cu_4X_4(dpmp)_4$ (X = I, Br, Cl; dpmp = 2-(Diphenylmethyl)pyridine), *Inorg. Chem.*, 1993, **32**, 869–874.

16 M. Vitale, W. E. Palke and P. C. Ford, Origins of the double emission of the tetranuclear copper(I) cluster $Cu_4I_4(pyridine)_4$: An ab initio study, *J. Phys. Chem.*, 1992, **96**, 8329–8336.

17 S. Masahara, H. Yokoyama, Y. Suzaki and T. Ide, Convenient synthesis of copper(I) halide quasi-one-dimensional coordination polymers: their structures and solid-state luminescent properties, *Dalton Trans.*, 2021, **50**, 8889–8898.

18 J. Conesa-Egea, F. Zamora and P. Amo-Ochoa, Perspectives of the smart Cu-Iodine coordination polymers: A portage to the world of new nanomaterials and composites, *Coord. Chem. Rev.*, 2019, **381**, 65–78.

19 M. J. Leitl, D. M. Zink, A. Schinabeck, T. Baumann, D. Volz and H. Yersin, Copper(I) Complexes for Thermally Activated Delayed Fluorescence: From Photophysical to Device Properties, *Top. Curr. Chem.*, 2016, **374**, 1–34.

20 S. Perruchas, Molecular copper iodide clusters: a distinguishing family of mechanochromic luminescent compounds, *Dalton Trans.*, 2021, **50**, 12031–12044.

21 D. M. Zink, L. Bergmann, D. Ambrosek, M. Wallesch, D. Volz and M. Mydlak, Singlet harvesting copper-based emitters: a modular approach towards next-generation OLED technology, *Transl. Mater. Res.*, 2014, **1**, 015003.

22 A. Kobayashi, T. Ehara, M. Yoshida and M. Kato, Quantitative Thermal Synthesis of Cu(I) Coordination Polymers That Exhibit Thermally Activated Delayed Fluorescence, *Inorg. Chem.*, 2020, **59**, 9511–9520.

23 A. V. Artem'ev, E. P. Doronina, M. I. Rakhmanova, X. Hei, D. V. Stass, O. A. Tarasova, I. Y. Bagryanskaya, D. G. Samsonenko, A. S. Novikov, N. A. Nedolya and J. Li, A family of CuI-based 1D polymers showing colorful short-lived TADF and phosphorescence induced by photo- and X-ray irradiation, *Dalton Trans.*, 2023, **52**, 4017–4027.

24 Z. Han, X. Y. Dong and S. Q. Zang, Crystalline Metal-Organic Materials with Thermally Activated Delayed Fluorescence, *Adv. Opt. Mater.*, 2021, **9**, 1–46.

25 V. W. W. Yam, V. K. M. Au and S. Y. L. Leung, Light-Emitting Self-Assembled Materials Based on d^8 and d^{10} Transition Metal Complexes, *Chem. Rev.*, 2015, **115**, 7589–7728.

26 F. Juvenal, A. Langlois, A. Bonnot, D. Fortin and P. D. Harvey, Luminescent 1D- and 2D-Coordination Polymers Using CuX Salts (X = Cl, Br, I) and a Metal-Containing Dithioether Ligand, *Inorg. Chem.*, 2016, **55**, 11096–11109.

27 M. Murillo, R. Wannemacher, J. Cabanillas-González, U. R. Rodríguez-Mendoza, J. Gonzalez-Platas, A. Liang, R. Turnbull, D. Errandonea, G. Lifante-Pedrola, A. García-Hernán, J. I. Martínez and P. Amo-Ochoa, 2D Cu(I)-I Coordination Polymer with Smart Optoelectronic Properties and Photocatalytic Activity as a Versatile Multifunctional Material, *Inorg. Chem.*, 2023, **62**, 10928–10939.

28 M. Yu, C. Liu, Y. Zhao, S. Li, Y. Yu, J. Lv, L. Chen, F. Jiang and M. Hong, White–Light Emission and Circularly Polarized Luminescence from a Chiral Copper(I) Coordination Polymer through Symmetry–Breaking Crystallization, *Angew. Chem.*, 2022, **134**, 1–6.

29 J. Troyano, J. Perles, P. Amo-Ochoa, J. I. Martínez, M. Concepción Gimeno, V. Fernández-Moreira, F. Zamora and S. Delgado, Luminescent Thermochromism of 2D Coordination Polymers Based on Copper(I) Halides with 4-Hydroxythiophenol, *Chem. – Eur. J.*, 2016, **22**, 18027–18035.

30 T. Yoneda, C. Kasai, Y. Manabe, M. Tsurui, Y. Kitagawa, Y. Hasegawa, P. Sarkar and Y. Inokuma, Luminescent Coordination Polymers Constructed from a Flexible, Tetradentate Diisopyrazole Ligand and Copper(I) Halides, *Chem. – Asian J.*, 2020, **15**, 601–605.

31 J. Chojnacki, M. Mońka, I. E. Serdiuk, P. Bojarski, T. Połoński and T. Olszewska, Copper(I) halide cluster-based coordination polymers modulated by chiral ditopic dithiodianthranilide ligands: Synthesis, crystal structure and photoluminescence, *CrystEngComm*, 2021, **23**, 299–307.

32 L. X. Hu, M. Gao, T. Wen, Y. Kang and S. Chen, Synthesis of Halide-Modulated Cuprous(I) Coordination Polymers with Mechanochromic and Photocatalytic Properties, *Inorg. Chem.*, 2017, **56**, 6507–6511.

33 J. Troyano, J. Perles, P. Amo-Ochoa, J. I. Martínez, F. Zamora and S. Delgado, Reversible recrystallization process of copper and silver thioacetamide-halide coordination polymers and their basic building blocks, *CrystEngComm*, 2014, **16**, 8224–8231.

34 A. Gallego, O. Castillo, C. J. Gómez-García, F. Zamora and S. Delgado, Electrical conductivity and luminescence in coordination polymers based on copper(I)-halides and sulfur-pyrimidine ligands, *Inorg. Chem.*, 2012, **51**, 718–727.

35 T. Zhang, C. Ji, K. Wang, D. Fortin and P. D. Harvey, First halogen anion-bridged $(MMX)_n$-type one-dimensional coordination polymer built upon d^{10}-d^{10} dimers, *Inorg. Chem.*, 2010, **49**, 11069–11076.

36 C. Zuffa, C. Cappuccino, M. Marchini, L. Contini, F. Farinella and L. Maini, {AgX}-based hybrid coordination polymers: mechanochemical synthesis, structure and luminescence property characterization, *Faraday Discuss.*, 2023, **241**, 448–465.

37 M. Dosen, Y. Kawada, S. Shibata, K. Tsuge, Y. Sasaki, A. Kobayashi, M. Kato, S. Ishizaka and N. Kitamura, Control of Emissive Excited States of Silver(I) Halogenido

Coordination Polymers by a Solid Solution Approach, *Inorg. Chem.*, 2019, **58**, 8419–8431.

38 J. Vallejos, I. Brito, A. Cárdenas, M. Bolte, S. Conejeros, P. Alemany and J. Llanos, Self-assembly of discrete metallocycles versus coordination polymers based on Cu(I) and Ag(I) ions and flexible ligands: Structural diversification and luminescent properties, *Polymers*, 2016, **8**, 1–16.

39 D. Yang, W. Xu, X. Cao, S. Zheng, J. He, Q. Ju, Z. Fang and W. Huang, Two Silver Coordination Network Compounds with Colorful Photoluminescence, *Inorg. Chem.*, 2016, **55**, 7954–7961.

40 A. Forni, E. Cariati, L. Carlucci, E. Lucenti, D. Marinotto, S. Pieraccini and M. Sironi, Interpreting the different emissive properties of cyclic triimidazole-based CuI and AgI coordination polymers: a QTAIM and IQA study, *Acta Crystallogr., Sect. B:Struct. Sci., Cryst. Eng. Mater.*, 2021, **77**, 865–870.

41 S. R. Batten, N. R. Champness, X. M. Chen, J. Garcia-Martinez, S. Kitagawa, L. Öhrström, M. O'Keeffe, M. P. Suh and J. Reedijk, Coordination polymers, metal-organic frameworks and the need for terminology guidelines, *CrystEngComm*, 2012, **14**, 3001–3004.

42 C. Zuffa, C. Cappuccino, L. Casali, F. Emmerling and L. Maini, Liquid reagents are not enough for liquid assisted grinding in the synthesis of $[(AgBr)(n\text{-pica})]_n$, *Phys. Chem. Chem. Phys.*, 2024, **26**, 5010–5019.

43 C. R. Groom, I. J. Bruno, M. P. Lightfoot and S. C. Ward, The Cambridge structural database, *Acta Crystallogr., Sect. B:Struct. Sci., Cryst. Eng. Mater.*, 2016, **72**, 171–179.

44 M. D. King, W. D. Buchanan and T. M. Korter, Application of London-type dispersion corrections to the solid-state density functional theory simulation of the terahertz spectra of crystalline pharmaceuticals, *Phys. Chem. Chem. Phys.*, 2011, **13**, 4250–4259.

45 M. A. Omary, T. R. Webb, Z. Assefa, G. E. Shankle and H. H. Patterson, Crystal Structure, Electronic Structure, and Temperature-Dependent Raman Spectra of $Tl[Ag(CN)_2]$: Evidence for Ligand-Unsupported Argentophilic Interactions, *Inorg. Chem.*, 1998, **37**, 1380–1386.

46 M. Puszynska-Tuszkanow, Z. Staszak, T. Misiaszek, M. T. Klepka, A. Wolska, A. Drzewiecka-Antonik, H. Faltynowicz and M. Cieslak-Golonka, Metallophilic interactions in polynuclear Ag(I) complex with 1-methylhydantoin studied by X-ray absorption, electronic and vibrational spectroscopies, *Chem. Phys. Lett.*, 2014, **597**, 94–98.

47 S. Dawn, S. R. Salpage, M. D. Smith, S. K. Sharma and L. S. Shimizu, A trinuclear silver coordination polymer from a bipyridine bis-urea macrocyclic ligand and silver triflate, *Inorg. Chem. Commun.*, 2012, **15**, 88–92.

48 D. Perreault, M. Drouin, A. Michel, V. M. Miskowski, W. P. Schaefer and P. D. Harvey, Silver and gold dimers. Crystal and molecular structure of $Ag_2(dmpm)_2Br_2$ and $[Au_2(dmpm)_2](PF_6)_2$ and relation between metal-metal force constants and metal-metal separations, *Inorg. Chem.*, 1992, **31**, 695–702.

49 C. M. Che, M. C. Tse, M. C. W. Chan, K. K. Cheung, D. L. Phillips and K. H. Leung, Spectroscopic evidence for argentophilicity in structurally characterized luminescent binuclear silver(I) complexes, *J. Am. Chem. Soc.*, 2000, **122**, 2464–2468.

50 X. Huang, H. Li, Z. Tu, L. Liu, X. Wu, J. Chen, Y. Liang, Y. Zou, Y. Yi, J. Sun, W. Xu and D. Zhu, Highly Conducting Neutral Coordination Polymer with Infinite Two-Dimensional Silver-Sulfur Networks, *J. Am. Chem. Soc.*, 2018, **140**, 15153–15156.

51 G. Ferraris, E. Makovicky and S. Merlino, Polytypes and polytype categories, *Crystallography of Modular Materials*, 2008, pp. 207–226.

52 B. B. Zvyagin, Polytypism of crystal structures, *Comput. Math. Appl.*, 1988, **16**, 569–591.

53 Y. M. Chumakov, O. Danilescu, O. V. Kulikova, P. Bourosh, I. Bulhac and L. Croitor, Metal ions impact on the isostructurality and properties of 2D coordination polymers, *CrystEngComm*, 2022, **24**, 4430–4439.

54 A. V. Artem'Ev, E. P. Doronina, M. I. Rakhmanova, O. A. Tarasova, I. Y. Bagryanskaya and N. A. Nedolya, Chemoselective mechanochemical route toward a bright TADF-emitting CuI-based coordination polymer, *Inorg. Chem. Front.*, 2019, **6**, 671–679.

55 I. L. Malaestean, V. C. Kravtsov, J. Lipkowski, E. Cariati, S. Righetto, D. Marinotto, A. Forni and M. S. Fonari, Partial in Situ Reduction of Copper(II) Resulting in One-Pot Formation of 2D Neutral and 3D Cationic Copper(I) Iodide-Pyrazine Coordination Polymers: Structure and Emissive Properties, *Inorg. Chem.*, 2017, **56**, 5141–5151.

56 X. Q. Liang, R. K. Gupta, Y. W. Li, H. Y. Ma, L. N. Gao, C. H. Tung and D. Sun, Structural Diversity of Copper(I) Cluster-Based Coordination Polymers with Pyrazine-2-thiol Ligand, *Inorg. Chem.*, 2020, **59**, 2680–2688.

57 A. Mensah, J. J. Shao, J. L. Ni, G. J. Li, F. M. Wang and L. Z. Chen, Recent Progress in Luminescent Cu(I) Halide Complexes: A Mini-Review, *Front. Chem.*, 2022, **9**, 1–7.

58 Y. Hasegawa, N. Sato, J. Hayashi, Y. Kitagawa and K. Fushimi, Thermo-Sensitive EuIII Coordination Polymers with Amorphous Networks, *ChemistrySelect*, 2021, **6**, 2812–2816.

59 D. Malpicci, E. Lucenti, A. Forni, D. Marinotto, A. Previtali, L. Carlucci, P. Mercandelli, C. Botta, S. Righetto and E. Cariati, Ag(I) and Cu(I) cyclic-triimidazole coordination polymers: Revealing different deactivation channels for multiple room temperature phosphorescences, *Inorg. Chem. Front.*, 2021, **8**, 1312–1323.

60 I. J. Bruno, J. C. Cole, P. R. Edgington, M. Kessler, C. F. Macrae, P. McCabe, J. Pearson and R. Taylor, New software for searching the Cambridge Structural Database and visualizing crystal structures, *Acta Crystallogr., Sect. B: Struct. Sci.*, 2002, **58**, 389–397.

61 G. M. Sheldrick, SHELXT - Integrated space-group and crystal-structure determination, *Acta Crystallogr., Sect. B: Struct. Sci., Cryst. Eng. Mater.*, 2015, **71**, 3–8.

62 R. Herbst-Irmer and G. M. Sheldrick, Refinement of Twinned Structures with SHELXL97, *Acta Crystallogr.*, 1998, **54**, 443–449.

63 A. A. Coelho, TOPAS and TOPAS-Academic: An optimization program integrating computer algebra and crystallographic objects written in C++, *J. Appl. Crystallogr.*, 2018, **51**, 210–218.
64 C. F. MacRae, I. Sovago, S. J. Cottrell, P. T. A. Galek, P. McCabe, E. Pidcock, M. Platings, G. P. Shields, J. S. Stevens, M. Towler and P. A. Wood, Mercury 4.0: From visualization to analysis, design and prediction, *J. Appl. Crystallogr.*, 2020, **53**, 226–235.
65 P. O. Löwdin, On the non-orthogonality problem connected with the use of atomic wave functions in the theory of molecules and crystals, *J. Chem. Phys.*, 1950, **18**, 365–375.
66 L. Fábián and A. Kálmán, Volumetric measure of isostructurality, *Acta Crystallogr., Sect. B:Struct. Sci.*, 1999, **55**, 1099–1108.
67 M. Che, J. C. Ve and E. J. Welzel, *Characterization of Solid Materials and Heterogeneous Catalysts*, 2012.
68 F. C. Jentoft, Ultraviolet–Visible–Near Infrared Spectroscopy in Catalysis: Theory, Experiment, Analysis, and Application Under Reaction Conditions, *Adv. Catal.*, 2009, **52**, 129–211.
69 C. Würth, M. Grabolle, J. Pauli, M. Spieles and U. Resch-Genger, Relative and absolute determination of fluorescence quantum yields of transparent samples, *Nat. Protoc.*, 2013, **8**, 1535–1550.
70 P. Giannozzi, S. Baroni, N. Bonini, M. Calandra, R. Car, C. Cavazzoni, D. Ceresoli, G. L. Chiarotti, M. Cococcioni, I. Dabo, A. Dal Corso, S. De Gironcoli, S. Fabris, G. Fratesi, R. Gebauer, U. Gerstmann, C. Gougoussis, A. Kokalj, M. Lazzeri, L. Martin-Samos, N. Marzari, F. Mauri, R. Mazzarello, S. Paolini, A. Pasquarello, L. Paulatto, C. Sbraccia, S. Scandolo, G. Sclauzero, A. P. Seitsonen, A. Smogunov, P. Umari and R. M. Wentzcovitch, QUANTUM ESPRESSO: A modular and open-source software project for quantum simulations of materials, *J. Phys.: Condens. Matter*, 2009, **21**, 1–19.
71 P. Giannozzi, O. Andreussi, T. Brumme, O. Bunau, M. Buongiorno Nardelli, M. Calandra, R. Car, C. Cavazzoni, D. Ceresoli, M. Cococcioni, *et al.*, Advanced capabilities for materials modelling with Quantum ESPRESSO, *J. Phys.: Condens. Matter*, 2017, **29**, 465901.
72 P. Giannozzi, O. Baseggio, P. Bonfà, D. Brunato, R. Car, I. Carnimeo, C. Cavazzoni, S. De Gironcoli, P. Delugas, F. Ferrari Ruffino, A. Ferretti, N. Marzari, I. Timrov, A. Urru and S. Baroni, Quantum ESPRESSO toward the exascale, *J. Chem. Phys.*, 2020, **152**, 154105.
73 J. P. Perdew, A. Ruzsinszky, G. I. Csonka, O. A. Vydrov, G. E. Scuseria, L. A. Constantin, X. Zhou and K. Burke, Restoring the density-gradient expansion for exchange in solids and surfaces, *Phys. Rev. Lett.*, 2008, **100**, 1–4.
74 S. Grimme, J. Antony, S. Ehrlich and H. Krieg, A consistent and accurate ab initio parametrization of density functional dispersion correction (DFT-D) for the 94 elements H-Pu, *J. Chem. Phys.*, 2010, **132**, 154104.
75 G. Prandini, A. Marrazzo, I. E. Castelli, N. Mounet and N. Marzari, Precision and efficiency in solid-state pseudopotential calculations, *npj Comput. Mater.*, 2018, **4**, 1–15.
76 K. Lejaeghere, G. Bihlmayer, T. Björkman, P. Blaha, S. Blügel, V. Blum, D. Caliste, I. E. Castelli, S. J. Clark, A. Dal Corso, S. De Gironcoli, T. Deutsch, J. K. Dewhurst, I. Di Marco, C. Draxl, M. Dułak, O. Eriksson, J. A. Flores-Livas, K. F. Garrity, L. Genovese, P. Giannozzi, M. Giantomassi, S. Goedecker, X. Gonze, O. Grånäs, E. K. U. Gross, A. Gulans, F. Gygi, D. R. Hamann, P. J. Hasnip, N. A. W. Holzwarth, D. Iuşan, D. B. Jochym, F. Jollet, D. Jones, G. Kresse, K. Koepernik, E. Küçükbenli, Y. O. Kvashnin, I. L. M. Locht, S. Lubeck, M. Marsman, N. Marzari, U. Nitzsche, L. Nordström, T. Ozaki, L. Paulatto, C. J. Pickard, W. Poelmans, M. I. J. Probert, K. Refson, M. Richter, G. M. Rignanese, S. Saha, M. Scheffler, M. Schlipf, K. Schwarz, S. Sharma, F. Tavazza, P. Thunström, A. Tkatchenko, M. Torrent, D. Vanderbilt, M. J. Van Setten, V. Van Speybroeck, J. M. Wills, J. R. Yates, G. X. Zhang and S. Cottenier, Reproducibility in density functional theory calculations of solids, *Science*, 2016, **351**, 1415–1423.
77 L. Talirz, S. Kumbhar, E. Passaro, A. V. Yakutovich, V. Granata, F. Gargiulo, M. Borelli, M. Uhrin, S. P. Huber, S. Zoupanos, C. S. Adorf, C. W. Andersen, O. Schütt, C. A. Pignedoli, D. Passerone, J. VandeVondele, T. C. Schulthess, B. Smit, G. Pizzi and N. Marzari, Materials Cloud, a platform for open computational science, *Sci. Data*, 2020, **7**, 1–12.
78 K. Momma and F. Izumi, VESTA 3 for three-dimensional visualization of crystal, volumetric and morphology data, *J. Appl. Crystallogr.*, 2011, **44**, 1272–1276.